Soft Matter

PAPER

View Article Online
View Journal | View Issue

Check for updates

Cite this: *Soft Matter*, 2024, **20**, 7502

Functional supraparticles produced by the evaporation of binary colloidal suspensions on superhydrophobic surfaces

Anna V. Shneidman,*[a] Cathy T. Y. Zhang,[a] Nikolaj K. Mandsberg,[b] Vittoria C. T. M. Picece,[acd] Elijah Shirman,[a] Gurminder K. Paink,[a] Natalie J. Nicolas[a] and Joanna Aizenberg*[ae]

Hierarchically structured supraparticles can be produced by drying droplets of colloidal suspensions. Using binary suspensions provides degrees of structural and functional control beyond those possible for single components, while remaining tractable for fundamental mechanistic studies. Here, we implement evaporative co-assembly of two distinct particle types – 'large' polystyrene microparticles and 'small' inorganic oxide nanoparticles (silica, titania, zirconia, or ceria) – dried on superhydrophobic surfaces to produce bowl-shaped supraparticles. We extend this method to raspberry colloid templating, in which the binary suspension consists of titania nanoparticles together with gold-decorated polystyrene colloids. Following removal of the polymer particles, we demonstrate catalytic oxidative coupling of methanol to methyl formate using the resulting mesoporous supraparticles, showcasing their practical application.

Received 19th April 2024,
Accepted 30th August 2024

DOI: 10.1039/d4sm00458b

rsc.li/soft-matter-journal

Published on 13 September 2024. Downloaded on 5/23/2026 4:22:31 AM.

Introduction

Supraparticles – micron to millimetre sized particles composed of self-assembled nanoscale constituents – are a fascinating and rich topic of research, which has seen numerous ground breaking insights and applications over the last two decades.[1] These developments are paving the way to innovations in drug delivery,[2–4] sensing,[5–8] catalysis,[9,10] energy storage,[11] filtration,[12] and photonics,[13–16] to name a few.

The implementation of supraparticles in practical applications requires the ability to produce them at scale with precisely designed composition, nanostructuration, and morphology. A common method of supraparticle preparation is evaporation-induced self-assembly (EISA) from droplet suspensions, whereby colloidal particles are advected to the receding evaporation front and are drawn together by capillary forces.[17] Extensive research of EISA of droplet suspensions containing one particle type has provided detailed fundamental insights into the particle self-assembly process.[18] On the other end of complexity, multicomponent suspensions are studied due to their practical relevance in a variety of applications including coatings, paints, and inks;[2,19] dairy and other food products;[20] drug delivery and pharmaceuticals;[21,22] and diagnostics and forensics.[23–26] The intermediate regime of only few particles is more tractable for theory, and unlocks new morphologies and functionalities beyond those possible for single particles.[27–29] Such systems provide the tools and insights to bridge the gap between fundamental research and practical applications across a broad range of disciplines.[20]

Herein, we perform fundamental studies of droplet-confined evaporative self-assembly of large polystyrene (PS) particles and small inorganic oxide nanoparticles (silica, titania, ceria, and zirconia) with a size ratio of ~18 : 1 (~360 nm and 20 nm in diameter, respectively). By varying the droplet content and substrate morphology, we develop mechanistic insights and ways to control the hierarchical structuration and overall shape of the resulting supraparticles. Furthermore, by selectively removing the PS component, we achieve mesoporous supraparticles, whose overall geometry, large accessible surface area, and highly interconnected pores make them especially interesting for advanced catalytic applications. Implementing hybrid organic/inorganic colloids, we produce a batch (57 mg) of supraparticles composed of titania and gold and apply them to the catalytic oxidative coupling of methanol to methyl formate. We envision the possibility of further optimization at the materials level, scaleup, and applications in photocatalysis and energy storage.

[a] *Harvard John A. Paulson School of Engineering and Applied Sciences, 150 Western Ave., Boston MA 02134, USA. E-mail: jaiz@seas.harvard.edu, ashneidm@g.harvard.edu*
[b] *Karlsruhe Institute of Technology (KIT) Institute of Biological and Chemical Systems – Functional Molecular Systems (IBCS-FMS) Kaiserstrasse 12, 76131 Karlsruhe, Germany*
[c] *Department of Chemistry, ETH Zurich, Vladimir-Prelog-Weg 1-5/10, 8093 Zurich, Switzerland*
[d] *Department of Materials, ETH Zurich, Leopold-Ruzicka-Weg 4, 8093 Zurich, Switzerland*
[e] *Department of Chemistry and Chemical Biology, Harvard Univeristy 12 Oxford St, Cambridge, MA 02138, USA*

This journal is © The Royal Society of Chemistry 2024

Published on 13 September 2024. Downloaded on 5/23/2026 4:22:31 AM.

Results

PS microparticles ('large particles') were synthesised using emulsion-free polymerization, while all inorganic oxide nanoparticles ('small particles') were purchased. In each case, the two particle types had similar surface charges to stabilise the suspension *via* electrostatic repulsion, thereby preventing uncontrolled disordered aggregation. Suspensions containing the two particle types were deposited in droplets of 3 μL on superhydrophobic (SH) substrates (Fig. 1A–C). The SH substrates were fabricated by soft-lithography, spin coated with a layer of alumina sol–gel and treated in boiling water to generate a boehmite (γ-AlO(OH)) coating with nanometer-scale roughness[30] (Fig. 1C). The substrate was then chemically functionalised by plasma deposition of perfluorocyclobutane (C_4F_8) to generate a superhydrophobic surface. The full procedures are detailed in the Experimental section. The droplet suspensions assumed a Cassie–Baxter state (did not infiltrate between pillars or into wells and had measured water contact angles of $\geq 150^\circ$). As the droplets maintained a nearly-spherical shape throughout evaporation, the resulting supraparticles had 3D – rather than flattened – shapes[28,31,32] (Fig. 1D and E). The supraparticles' colour, evident in Fig. 1D, is structural colour, governed by light scattering from materials with differing refractive indices (*i.e.*, ~1.59 and ~1.45 for bulk PS and SiO_2, respectively).[33] The iridescence arises from periodic packing of the larger particles, whose size is commensurate with wavelengths of visible light, while the white/pearlescent quality is due to scattering of light from partially or fully disordered regions. Under ambient conditions (room temperature and pressure, and relative humidity of ~20%), complete evaporation of the 3 μL droplet suspensions occurred within 15–20 min, producing supraparticles such as the one shown in Fig. 1D–F. Here, the SH substrates consisted of a hexagonal array of epoxy pillars providing micrometre-scale patterning at 6% solid coverage. The droplets initially contained 3.6 vol% of PS and 1.7 vol% of SiO_2, corresponding to relative volumes of 68% and 32% for the large and small particles, respectively (see Experimental section for calculation of relative volumes). The proportion of small particles was chosen to fill the interstitials between the large ones in the final supraparticles, assuming the large particles occupy a slightly less dense packing than close packing for monodisperse spheres, *i.e.*, a face-centered cubic packing (fcc), where the interstitials account for 26% of the volume, but more dense than random close packing, where the interstitials account for 36% of the total volume. This assumption was made to account for the frustrated particle packing caused by the curvature of the interface, the presence of voids between the nanoparticles, and the non-crystalline packing during the final stages of drying, as described below.

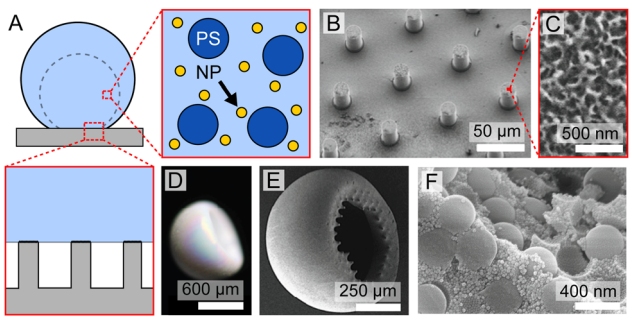

Fig. 1 Droplet suspensions evaporating on a superhydrophobic (SH) surface. (A) Schematic illustrating the drying process. The receding droplet front is indicated by the dotted line. The images with red borders provide zoom-ins to (bottom) the micron-scale epoxy pillars on the substrate and (right) the colloidal suspension consisting of larger polystyrene (PS, dark blue) and smaller inorganic oxide nanoparticles (NPs, yellow). (B) Scanning electron microscopy (SEM) image of a microstructured superhydrophobic substrate featuring epoxy microposts coated with (C) nanostructured aluminum oxide hydroxide (boehmite, γ-AlO(OH)) and functionalised by plasma deposition of perfluorocyclobutane. (D)–(F) Typical supraparticle resulting from evaporation of a droplet suspension on such a substrate. The optical microscopy image (D) and SEM images (E) and (F) reveal its micro- and nanoscale morphologies. The initial drop size was 3 μL, consisting of 3.6 vol% PS and 1.7 vol% SiO_2.

We observed that the overall EISA process for binary droplet suspensions resembled that of single-particle systems, consisting of either the small or large particles alone, and can be described by a four-stage process[34,35] (Fig. 2): (1) isotropic droplet shrinkage, followed by (2) particle accumulation at the periphery of the droplet in an ordered fashion. As water evaporates, menisci are formed in the interstitial spaces between the particles at the air–water interface. Capillary forces arise from the curvature of the menisci, driving the particles together and the fluid outward.[36] This leads to (3) particle jamming and an associated viscoelastic transition, whereby the shell can be described as an elastic membrane. This membrane buckles to release the tensile stresses imposed on the shell by capillary forces.[36,37] Buckling occurs at the weakest spot on the shell, which, for the substrate in question, is at the bottom where adhesion is sparse due to the pillar distance. This delineates the onset of "rush-hour," a fast evaporation stage in which advection outpaces diffusion such that the colloidal particles remaining in the bulk of the droplet do not have time to self-organise and therefore accumulate in a disordered inner layer.[38] (4) The remaining water evaporates, leaving behind a fully-formed supraparticle, which might partially detach from the surface, 'jump off', and/or crack, all of which are influenced by the interparticle forces as well as the adhesion to and deformability of the substrate.[39]

An immediately observable difference between the binary and unary droplet suspensions is at stage 2. In the binary system, the larger particles organise in an approximately fcc lattice and smaller particles accumulate within the interstitials between them.† This observation is in line with the

† Other particle organisations are possible for the binary suspensions. For example, at low humidity, particles of 3 μm and 300 nm have been shown to adopt an "inverse stratification," where the smaller particles accumulate at the periphery.[40] Such arrangements were not observed in our case as the 'large' and 'small' particles both have Péclet numbers $\gg 1$ in the regimes tested. Segregation of particles by size ('nanochromatography') has also been observed for droplets drying on hydrophilic surfaces, where the capillary forces dominate over interparticle and particle–substrate forces,[41,42] and was not observed here, with the droplets maintaining $a \geq 150^\circ$ contact angle with the surface throughout the drying process.

Published on 13 September 2024. Downloaded on 5/23/2026 4:22:31 AM.

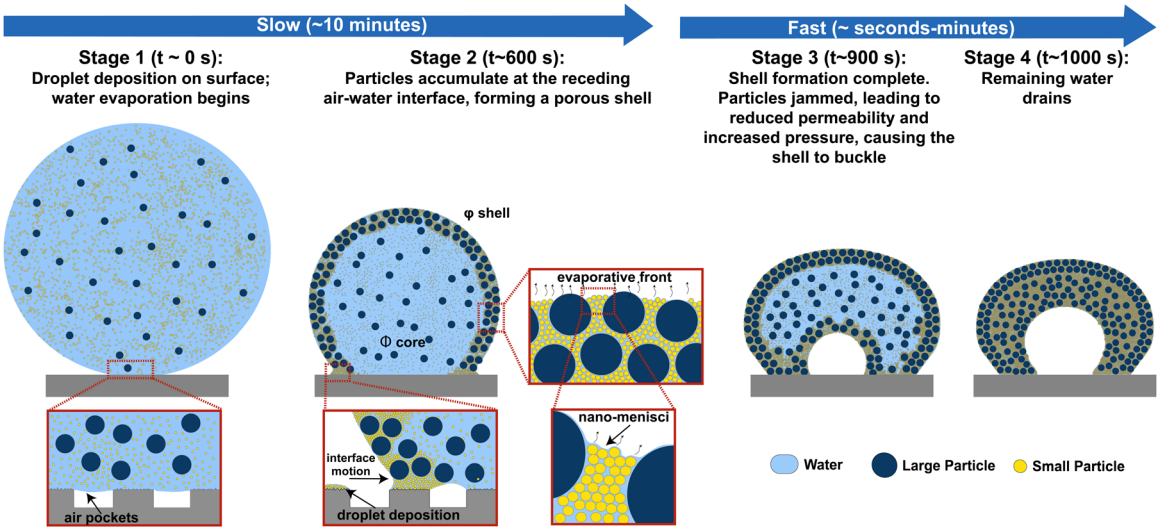

Fig. 2 Schematic illustrating the mechanism of supraparticle formation from the evaporation of a binary colloidal sessile droplet consisting of 2 species of particles with diameter ratio exceeding 10 : 1. Times *t* indicate approximate start times of each stage. The drawing is not to scale; in particular, the ratio of particle to droplet size is much smaller than pictured. The times included parenthetically correspond to the values obtained for 3 μL binary droplets consisting of 3.6 vol% PS and 1.7 vol% SiO_2 at ambient conditions (room temperature and pressure, and a relative humidity of ~20%).

experimental and theoretical investigations performed in the case of thin film formation by EISA.[43,44] However, the film system presents several key differences: (1) the substrate is hydrophilic to promote wetting, leading to particle accumulation at the evaporating front near the substrate due to the meniscus curvature and (2) there is no shell formation and thus, the evaporation rate remains roughly constant throughout the thin film production process.

To investigate the effects of implementing a binary *vs.* unary suspension in more detail, we imaged the evaporating droplets from the side using a goniometer setup, allowing us to quantify the temporal evolution of the droplet height, central radius, base radius, and contact angle (Fig. 3A). We also visualised the droplet-surface contact over time using interference reflection microscopy,[30] from which we were able to quantify the number of droplet pinning sites (Fig. 3B). Three suspensions were compared. The 'base' case consisted of droplets containing 3.6 vol% PS only, resulting in purely PS supraparticles. The second suspension contained 1.7 vol% SiO_2 in addition to the 3.6% PS, to study how the drying dynamics change upon adding small particles. The third suspension was a control consisting of the same vol% of solids as the second, but containing no large particles, *i.e.* 5.3 vol% SiO_2. We found that the presence of the smaller particles influenced both the dynamics of the drying process and the morphology of the resulting supraparticles. Specifically, as they are on the same length scale as the boehmite nanoscale roughness, the SiO_2 particles aggregated on the tops of substrate pillars during evaporation, leading to pinning of the droplet edge until the end of evaporation, preventing reduction in the droplet base radius; note that the pinning increased with increasing concentration of the smaller particles (Fig. 3C). Additionally, we extracted the time to buckling (stage 3 in Fig. 2) from the side-view videos, defined as the moment of sharp increase in

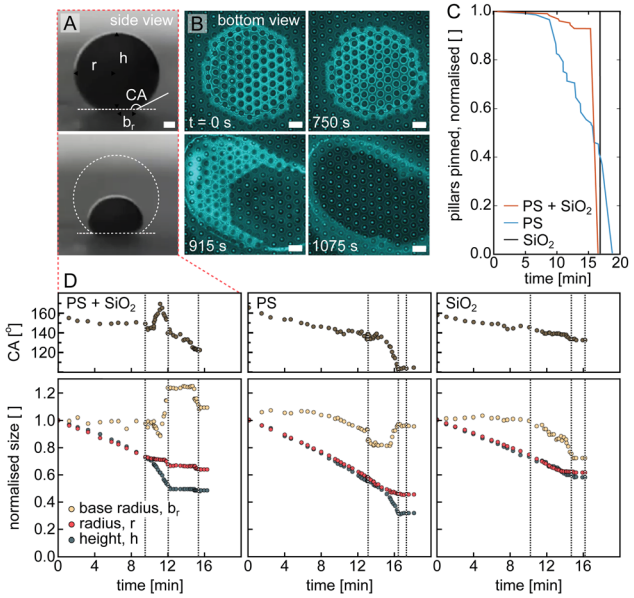

Fig. 3 Influence of smaller particles on both the drying process and the final morphology of the binary system. (A) Side-view camera image of an aqueous droplet suspension of 3.6 vol% PS and 1.7 vol% SiO_2 on the superhydrophobic surface, (top) before (t_{evap} = 0 s) and (bottom) after complete drying (t_{evap} = 1000 s). The droplet height (h), central radius (*r*), and base (radius) were recorded over the course of evaporation. (B) Bottom view reflectance interferometry visualization of the intercalated air film on the structured superhydrophobic surface. The contact area of the droplet with the surface is shown as bright cyan whereas the dark zones show regions where the surface is exposed to air. The anisotropic drop footprint at later times is likely due to random inhomogeneities on the surface, leading to a lower surface adhesion force on the right, where the droplet lifts up, accommodating faster evaporation from that side. (C) Depinning plots of the three analyzed suspensions (3.6% PS + 1.7% SiO_2, 3.6% PS, and 5.3% SiO_2). (D) Contact angles and normalised droplet dimensions versus the evaporation time. The different stages of the evaporative process are indicated by the dotted lines. All scale bars, 200 μm.

This journal is © The Royal Society of Chemistry 2024

Published on 13 September 2024. Downloaded on 5/23/2026 4:22:31 AM.

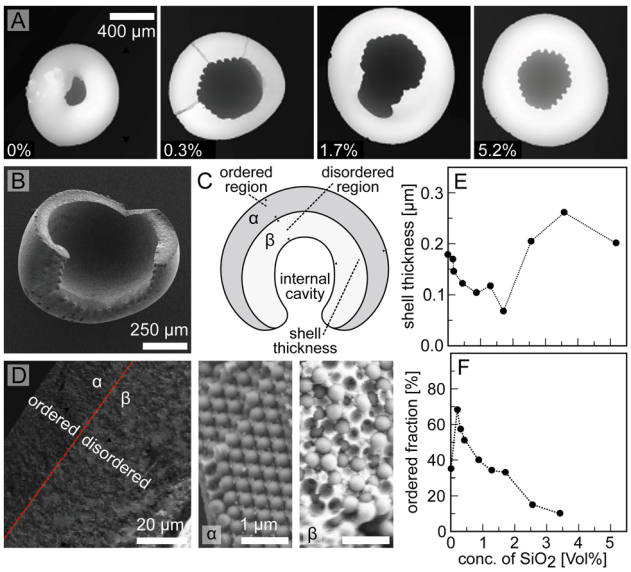

Fig. 4 Details of the supraparticle shell. (A) Topological rendering of a supraparticles bowl-side up for fixed PS (3.6 vol%) and varying SiO_2 volume fractions in the initial droplet, as indicated on each image. Confocal microscopy in reflection mode was used for imaging. (B) SEM micrograph of the final 3D morphology of a supraparticle resulting from a 3.6 vol% PS + 1.7 vol% SiO_2 droplet suspension. (C) Schematic illustrating the structural features of the supraparticles after complete evaporation. (D) SEM indicating the two different regions of the shell, with the dotted red line delineating the interface between them. The higher magnification SEM images show the closed-packed arrangement of the colloids in the outer part of the shell (α) and a disordered arrangement in the inner region (β). (E) Shell thickness for increasing concentrations of silica in the deposited droplet at a constant PS concentration of 3.6 vol%. (F) Percentage of the ordered shell region throughout the thickness of the shell for various concentrations of silica at a constant PS concentration of 3.6 vol%.

the rate of droplet height reduction (Fig. 3D). Formation of a shell began earlier for the binary droplet than for either of the unary systems primarily due to the higher packing fractions achieved for the binary mixtures with the smaller particles occupying the interstitials between the larger ones, thereby decreasing the permeability of the shell consisting of particles accumulating at the receding droplet front. The densification of the SiO_2 particles between the larger PS particles during the final stages of drying also stiffens and mechanically stabilises the shell.[45]

We examined the shell in more detail using confocal microscopy in reflection mode (Fig. 4A) and employed SEM for quantitative measurements of the shell thickness and its stratification; in SEM, the outer ordered region (α) appeared darker grey compared to the inner disordered region (β) (Fig. 4B–D). Details of the microscopy are provided in the Experimental section. For these studies, we kept the PS at 3.6 vol% and progressively increased the concentration of SiO_2, As the SiO_2 content increased from 0 to 1.7 vol%, the time to buckling decreased, resulting in wider and taller structures with thinner shells; increasing the concentration of SiO_2 still further resulted in an increase in total shell thickness (Fig. 4E). The nonmonotonicity in the total shell thickness arises from the nonmonotonicity of the packing density of binary systems, wherein the packing density first increases with increasing number of smaller particles in the interstitials between larger ones, and then decreases when the concentration of smaller particles exceeds a critical value and they begin to wedge the larger ones apart, preventing their optimal packing.[46,47] The permeability of the shell decreases with increasing packing density, leading to higher internal pressures and thus earlier buckling times. Meanwhile, the ordered fraction of the shell, defined as $\frac{\alpha}{\alpha+\beta} \times 100\%$, peaks for very low (but nonzero) SiO_2 concentrations and then steadily decreases (Fig. 4F).

The concentrations and types of particles determine the capillary forces acting on the shell and its bending modulus, while the interaction with the substrate dictates the adhesion force experienced by the shell at its base. Modifications to the surface structuration affect both the distribution of pinning sites and the vapour transport, ultimately affecting the overall supraparticle shape (Fig. 5, top row). Several superhydrophobic substrates were tested, including pillars and wells of varying radii (and therefore different solid fractions), as well as flat substrates (Fig. 5, bottom row). Substrates with relatively large solid fractions, for example, provided a large surface area over which particles could attach, thus producing a large adhesion force at the bottom. This shifted the weakest point of the nascent shell away from the base, leading to a larger occurrence of buckling from the top to form 'dimples' rather than cavities. In the limit where the microstructuration was eliminated (a flat substrate with only nanoscale roughness provided by boehmite), no gas transport was possible through the bottom of the droplet, resulting in advection predominantly away from the substrate, and, thus, limited particle deposition at the bottom. Thus, while surface adhesion of particles did increase, the particle flux to the bottom was suppressed, leading to supraparticles with thin, but well-adhered bases. For this substrate, buckling typically occurred at the top surface, creating dimples rather than internal cavities. When the pillars were replaced by holes (wells), evaporation could proceed through the bottom initially but quickly saturated as the wells trapped air without allowing gas transport between them. Initially, buckling predominantly occurred from the top, but as the surface area occupied by wells increased (*i.e.* solid fraction decreased), cavity formation at the base was restored.

EISA is a flexible process, in which the composition can easily be changed as long as the inter-particle forces are maintained.[48] We employed suspensions consisting of PS particles and titania, ceria, or zirconia nanoparticles (amidine-capped PS colloids were prepared to maintain charge-stabilisation for the positively charged nanoparticles). Importantly, the PS colloids could be removed to form highly porous inverse opal structures (IOs) (Fig. 6A), which have potential applications as structurally coloured 'pigments', sensors, adsorbents, and photo or thermal catalysts.[10]

Moreover, in different systems, our group has previously demonstrated catalytic mesoporous particles made by 'raspberry colloidal templating' (RCT), in which PS colloids are first

Published on 13 September 2024. Downloaded on 5/23/2026 4:22:31 AM.

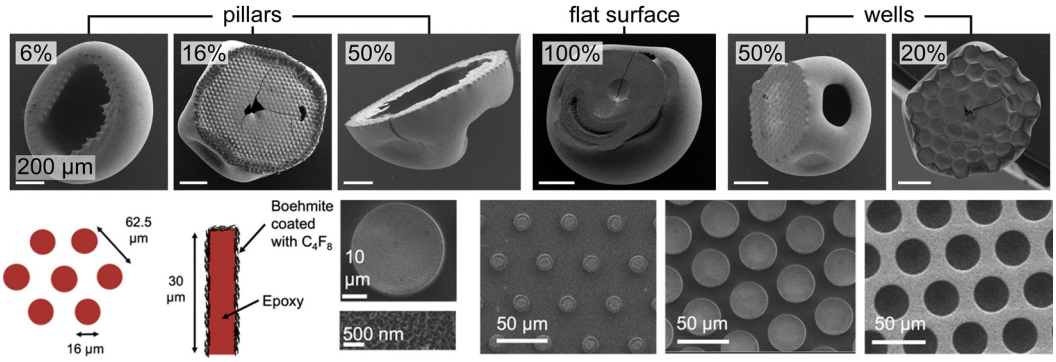

Fig. 5 (Top row) SEMs of 3.6 vol% PS + 1.7 vol% SiO_2 supraparticles assembled on SH substrates featuring different micro-scale surface patterns. The percentages on each image indicate the solid fraction of the corresponding substrate. (Bottow row) Examples of SH substrates used in the studies. Schematics show the top- and side-view of a pillar substrate with a ~6% surface fraction with a boehmite nano-texture coating. The SEMs show epoxy substrates with boehmite coatings. From left to right: a high magnification view of a single pillar above a zoom-in to the boehmite coating on its top surface; 6% pillar substate; 50% pillar substrate; 50% well substrate. For the pillar surfaces, surface fraction is calculated as the area of 3 pillars, each with radius r (*i.e.* center pillar + 6* 1/3 pillars enclosed in the unit cell) divided by the area of the hexagon with side given by d, the center-to-center distance between pillars, *i.e.* $3 \times \pi \times r^2/(3\sqrt{3} \times d^2/2)$. For example, in the case of the schematic, the surface fraction is $3 \times \pi \times 8^2/(3 \times \sqrt{3}) \times (62.5^2/2)$ = 5.9%.

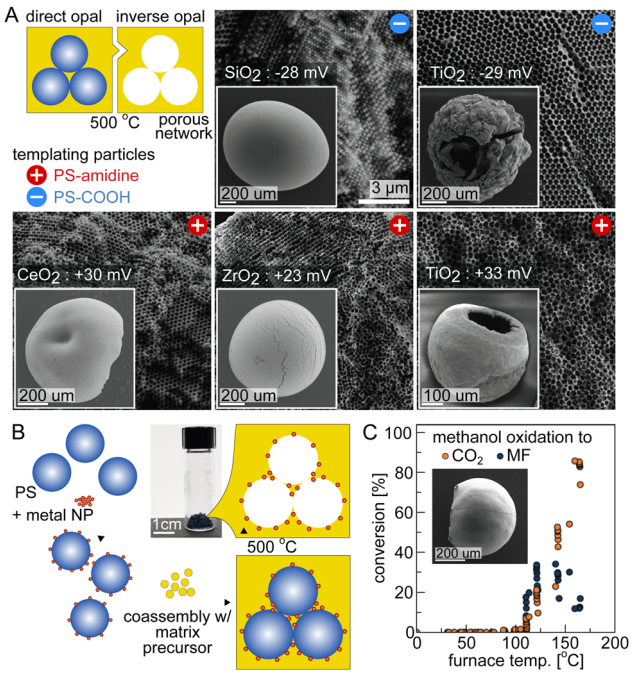

Fig. 6 Expanding the materials palette of supraparticles produced from droplet suspensions using (A) different inorganic oxide nanoparticles and (B) co-assembly with raspberry colloids. (A) Schematic and SEM images of invese opals consisting of silica, titania, or zirconia matrices. Insets show example supraparticles obtained for each inorganic oxide. Two types of titania were employed, with positive and negative surface termination. The red and blue circles on the top-right corner of the SEMs indicate which PS particles were used in the droplet suspension. (B) Schematics of the raspberry colloid templating (RCT) process: PS particles modified with metal nanoparticles (NPs) are co-assembled with the inorganic oxide precursor after which the polymeric template is removed through heat treatment, yielding inverse opals featuring metal NPs located at the matrix/pore interface. The photograph on the right shows a glass vial containing 57 mg of catalyst. (C) Oxidative coupling of methanol to methyl formate on TiO_2–Au catalyst such as the one shown in the inset. Full oxidation to CO_2 occurs as the temperature increases.

decorated with catalytic nanoparticles and then assembled on their own or together with inorganic oxide precursors (Fig. 6B, schematic).[49–51] The advantages of this approach, compared to the standard methods used in industry, is the especially high stability of the catalytic nanoparticles and high interconnectedness of the porous network, together providing unprecedented accessibility of the nanoparticles to reactants. The beneficial effects in terms of the catalytic nanoparticles are due to their unique positioning as a result of implementing RCT: they are anchored at the pore-matrix interface, maximising their exposure to the reactants while preventing them from sintering.[49,51] Meanwhile, the interconnected pores result from the ordered positioning of the templating spheres. To demonstrate this approach in the sessile droplet system, we prepared the RCT binary droplet suspension consisting of (1) PS particles decorated with the catalytic metal nanoparticles (instead of bare PS particles), together with (2) inorganic oxide nanoparticulate or other (*e.g.* sol–gel) precursor. Following evaporation, the resulting RCT supraparticles were calcined to form the mesoporous IO network with catalytic nanoparticles exposed on its surfaces. To scale-up the process and illustrate the potential of such RCT supraparticles in catalysis, a total of 57 mg of Au–TiO_2 supraparticle IOs were prepared (Fig. 6C, photograph). The Au–TiO_2 combination is valuable to various applications in plasmonics, photocatalysis, and thermal catalysis.[52–54] This material combination has also been implemented for delayed photocatalysis, in which electrons generated by light absorption in TiO_2 are transferred to Au, where they are stored until a reductant is present and reactions can proceed. We recently found that the charge-storage capacity of this system depends on the surface faceting of the constituent anatase TiO_2 nanocrystals.[55] Implementing the most active nanocrystals together with tuning the micro- and macro-structuration as described here, may allow us to further improve the propensity for delayed photocatalysis. As proof-of-concept, the RCT Au–TiO_2 supraparticles were implemented in the oxidative coupling of methanol to methyl

 This journal is © The Royal Society of Chemistry 2024

Published on 13 September 2024. Downloaded on 5/23/2026 4:22:31 AM.

formate (MF), with full oxidation to CO_2 becoming more prevalent at higher temperatures (Fig. 6C). MF is an important C1 synthetic precursor and further optimization of the geometry and materials (such as implementing metal alloys rather than Au alone) could vastly improve the yield while reducing the operating temperature.

Conclusions

In summary, multiple parameters can be tuned to shape the supraparticles that result from EISA of droplet suspensions. Here, we demonstrated that for a given substrate and ambient conditions (temperature, pressure, humidity), changing the concentration of smaller particles affects the overall thickness of the shell and relative ordered proportion. The SH surface plays a critical role in shaping the resultant supraparticles, as there is a competition between surface adhesion and capillary forces which exert stresses on the forming elastic membrane. We extended the results to a range of inorganic oxides and also incorporated metallic nanoparticles by using a raspberry templating approach, for which we demonstrated initial catalytic activity.

It will be interesting through future work to explore other means of morphological tuning, including adding salts to mediate interparticle forces and exploring other evaporation regimes, *e.g.* by changing the humidity or temperature. The asymmetric shape of the supraparticles allows them to act as macroscopic Janus particles. They can further be functionalised differently on the two sides, resulting in a cavity that is either more or less hydrophobic than the outer part of the supraparticle, which can be useful in filtration and photo-catalytic applications or for motile particles.[56,57] Additional asymmetry could be imposed by depositing the droplet on a stretched elastic substrate and releasing the tension at a rate commensurate with the evaporation time.

Using droplets to create supraparticles allows us to sharply reduce the timescales of drying and assembly as compared to thin film deposition ($\sim$15–20 min for drops compared to $\sim$3 days for films). This assembly method also is materials efficient, as essentially all of the constituent particles in the drop become part of the supraparticle. Assembly from sessile droplets altogether has a high potential for scaleup, as it can be parallelised using processes such as roll-to-roll or inkjet printing and is also highly modular with respect to materials if the evaporation rate, size, and surface charge of particles are consistent. In addition to the inorganic oxides analysed in this study, the material's toolbox can be expanded to include materials such as polyoxometalates, zeolites, and metal organic frameworks; or to conductive materials like carbon, metals, or indium-tin oxide. Furthermore, to enable multiple simultaneous catalytic reactions, different types of raspberry colloids could be implemented on a single matrix support.

Experimental

Materials

Styrene, acrylic acid, ammonium persulfate (APS), hydrochloric acid (HCl, aq., 36.5–38.0% w/w and 0.1 M), nitric acid (HNO_3, aq., 65% w/w), gold(III) chloride solution ($AuCl_3$, 30 wt% in diluted HCl), chloroauric acid trihydrate ($HAuCl_4{\cdot}3H_2O$), palladium(II) nitrate dihydrate ($Pd(NO_3)_2{\cdot}2H_2O$), chloroplatinic acid hexahydrate ($H_2PtCl_6{\cdot}6H_2O$), sodium citrate, sodium borohydride ($NaBH_4$), polyvinylpyrrolidone (PVP, MW: 10 000 g mol^{-1}), 2,2′-azobis(2-amidinopropane) dihydrochloride (AAPH), 2-aminoethanethiol hydrochloride (AET), *N*-ethyl-*N*′-(3-(dimethylamino)-propyl)carbodiimide hydrochloride (EDAC) and 2-(morpholino)ethanesulfonic acid (MES), toluene, methanol, and silica (SiO_2) nanoparticles (LUDOX TM40), aluminium tri-*sec*-butoxide, ethyl acetoacetate were purchased from Sigma-Aldrich. Ethanol (100%) and isopropanol (100%) were purchased from VWR, part of Avantor. SU-8 2035 was acquired from Microchem, Inc., Norland Optical Adhesive 61 (NOA 61) from Norland Products, Inc. Cerium(IV) oxide (CeO_2, CeO_2(AC)), zirconium dioxide (ZrO_2, Zr10/15), titanium dioxide (TiO_2, TiSolA, TiSol-NH_4) nanoparticles were purchased from Nyacol Nanotechnologies, Inc. Deionised (DI) water (Milli-Q, Millipore Sigma, 18 mΩ) was used for all the experiments. All chemicals were used as received, without any further purification or modification. All glassware and Teflon-coated magnetic stir bars used for the metal nanoparticle synthesis were cleaned in aqua regia (1 : 3 HNO_3 : HCl) and rinsed with DI water before use.

Equipment

Scanning electron microscopy (SEM) images were acquired using FESEM Ultra55, Supra55 VP and Ultra Plus (Zeiss). To image their cross-sections, supraparticles were cut under a dissecting microscope (*i.e.* a stereo microscope, Vision Engineering, Mantis Elite). Supraparticles were coated with 5 nm Pt : Pd (80 : 20) using a sputterer (Quorum Technologies, EMS 300T D) prior to imaging. Elemental compositions of nanoparticle (NP) solutions and the NP loading on the raspberry colloids were determined using inductively coupled plasma mass spectrometry (ICP-MS) measurements (Agilent Technologies 7700 Series). The zeta potentials and hydrodynamic diameters of all particles were measured through dynamic light scattering, DLS (Zetasizer Nano ZS, Malvern Analytical) and are reported in Tables 1 and 2. The concentration were verified *via* thermogravimetric analysis (TGA) (Discovery series, TA Instruments). Contact angles of droplets were measured using a goniometer (CAM 101, KSV Instruments). Substrate fabrication required plasma cleaning (Femto PCCE, Diener electronic), photolithography (uPG501, Heidelberg Instruments) and inductively coupled plasma reactive ion etching (ICP RIE-8, Surface Technology Systems). Confocal microscopy imaging

Table 1 Hydrodynamic diameters and zeta potentials of the small particles implemented in this work, measured *via* dynamic light scattering (DLS)

Oxide	Hydrodynamic diameter [nm]	ζ-Potential [mV]
SiO_2	22	−28.3 ± 1
CeO_2	21.0 ± 4.9	29.9 ± 2.8
ZrO_2	24.6 ± 1.8	22.3 ± 0.7
$TiO_2^{\oplus}$	34.5 ± 10.1	33.0 ± 3.4
$TiO_2^{\ominus}$	26.5 ± 0.8	−29.1 ± 2.4

Published on 13 September 2024. Downloaded on 5/23/2026 4:22:31 AM.

Table 2 Hydrodynamic diameters and zeta potentials of the large particles implemented in this work, measured *via* DLS. The subscript in the first 2 rows indicates the surface termination imposed on the PS during synthesis. PS-Au are PS particles decorated with Au nanoparticles

Colloid	Hydrodynamic diameter [nm]	ζ-Potential [mV]
PS_{COOH}	390	-43.4 ± 1.5
$PS_{amidine}$	350	39.2 ± 2.8
PS-Au	280	32.7 ± 2.5

and reflection interferometry[30] were performed on a laser scanning confocal microscope from Zeiss (LSM 700, Axio Imager M2) and on an inverted broadband confocal microscope from Leica (TCS SP5). Porous supraparticles were made using a furnace (Lynberg/Blue M). Catalytic activity was calculated using the reaction products measured by an online gas chromatograph (Agilent 7890A series, Column HP-Plot/Q) coupled with a mass spectrometer (Agilent 5975C series, inert MSD with triple-axis detector).

Fabrication of the superhydrophobic (SH) substrates

Substrates with different topographies (pillars, wells, and flat) and different surface fractions were fabricated using photolithography and reactive ion etching followed by replica moulding. First, silicon wafers (University Wafers, Inc.) were plasma cleaned (50% O_2 in Ar, 50 W, 5 min), after which the negative photoresist SU-8 2035 was spun-coated on top and the negative pattern was written using a direct write system. The resulting structures were replicated into NOA 61, spin coated with an alumina sol–gel and were treated at 100 °C in boiling water to form boehmite nanostructure on the pillars.[58] The samples were then functionalised with a thin coating of C_4F_8 using an ICP RIE system (flow rate of 120 sccm for 8 s under 1 mTorr pressure and 600 W coil and 0 W platen powers, respectively).

Alumina sol–gel preparation for substrate coating

Following a published procedure,[59] 3 g of aluminium tri-*sec*-butoxide was mixed with 30 mL of isopropyl alcohol while stirring. 2 mL of ethyl acetoacetate was then added after 10 min of stirring. After an additional 1 h of stirring, 6 mL of 5 : 1 IPA : H_2O was slowly added and the mixture was stirred for 1 h.

Synthesis of polystyrene colloids

Carboxylate-terminated polystyrene (PS-COOH). Monodisperse PS-COOH colloidal particles were synthesised through surfactant-free emulsion polymerization of styrene and acrylic acid in presence of APS as an initiator.[13] The average particle hydrodynamic diameter was 390 nm for the experiments employing PS-COOH. The copolymerization of the acrylic acid to the styrene introduces carboxylate surface groups, making the nanoparticles hydrophilic and therefore possible to disperse in water. The final diameter of the colloids is controlled by tuning the initial concentration of styrene and APS. After completion of the reaction, the final dispersion was purified through extensive dialysis. In all cases, the colloid size polydispersity was measured by DLS to be below 2%.

Amidine-terminated polystyrene (PS-amidine). Monodisperse PS-amidine particles (average hydrodynamic diameter: 350 nm) were synthesised in an emulsifier-free emulsion polymerization of styrene in presence of AAPH as an initiator following a literature procedure.[60] The mixture was stirred at 80 °C under reflux for 24 h. After reaction completion, the dispersion was purified through extensive dialysis.

Thiol-modified polystyrene (PS-thiol). Thiol modification of PS-COOH was performed according to a modified literature procedure.[49,61] PS-COOH colloids (average hydrodynamic diameter: 280 nm; 10 mL of 1 wt%) were dispersed in 0.5 mL of 500 mM MES buffer solution, following which 4.4 mL of EDAC was added (52 mM) while stirring. 25 mg of AET in 0.5 mL of water was added 30 min later.

Synthesis of gold nanoparticles

Dispersions of citrate-stabilised Au nanoparticles were synthesised following a modified literature procedure.[62] 1 mL of 1% tri-sodium citrate aqueous solution was added to a stirring solution composed of 10 mg of $HAuCl_4$ in 100 mL of H_2O. After 1 min, 1 mL of 0.075% $NaBH_4$ in 1% tri-sodium citrate was added to the reaction mixture and the solution was stirred for 5 min.

Synthesis of raspberry colloids

Raspberry colloids (Au on PS) were synthesised by addition of a specific amount of metallic NPs to the respective PS solution (PS-thiol). This mixture was stirred, washed at least 3 times using centrifugation and sonication, and redispersed in DI water to give the desired concentration of particles (wt%).[49,50]

Preparation of colloidal suspensions and droplet deposition

PS or raspberry colloids and inorganic oxide nanoparticles were dispersed in DI water and sonicated (Bransonic M5800, Branson) to evenly disperse the nanoparticles in solution. 3 μL droplets were deposited on the substrate through the use of a superhydrophobic glass capillary connected to a syringe pump (PHD Ultra, Harvard Apparatus). After deposition of the first droplet, further droplets were spaced at least 5 mm apart from each other, to ensure no interactions between adjacent droplets.[31,63]

Calculation of relative volume fraction of each type of particle

The relative volume fraction occupied by each type of particle is defined as: $f_i \equiv \frac{V_i}{V_s + V_l}$, where subscripts s, l correspond to small and large particles, respectively, and $V_i = N_i \frac{4\pi}{3} r_i^3$ is the total volume occupied by N_i number of particles of type $i = s, l$, having radius of r_i.

Creation of porous supraparticles

After drying, the co-assembled supraparticles were removed from the surface and calcined in air at a temperature of 500 °C to remove the PS particles and partially sinter the metal oxide.

 This journal is © The Royal Society of Chemistry 2024

Published on 13 September 2024. Downloaded on 5/23/2026 4:22:31 AM.

Imaging and quantification of shell thickness

The supraparticles were placed on a glass slide, cavity-side up, and imaged using confocal microscopy in reflection mode. The TopoJ plugin was then used to render the images and ImageJ measuring tool was used to quantify the shell thickness.

Quantification of shell's ordered fraction

Supraparticles were attached to an SEM stub (Ted Pella, PELCO 16111) with carbon tape (Ted Pella, PELCO Image Tabs) and sliced open under a stereo microscope, 10X magnification, using a razor blade. Those that were cut roughly at the midpoint of the 'bowl' were imaged with SEM following deposition of 5 nm Pt/Pd. Measurements of $\alpha + \beta$ (total shell thickness) and well as α alone (thickness of the ordered region) were taken in ImageJ at the midpoint between the apex and base of the bowl. These measurements were taken for 3 supraparticles formed at the same conditions, and the mean and standard deviation are reported.

Catalytic experiments

A custom fixed-bed microreactor at atmospheric pressure was used for the catalytic experiments. The supraparticles ($\sim$30 mg) were diluted with quartz sand (roughly 3 : 1 v : v sand : catalyst) before loading into the quartz reactor tubes (custom made by Finkenbeiner.com, 0.5″ diameter, embedded quartz frit). The temperature was set using a proportional-integral-derivative (PID) controller (The Mellen Company Inc., NH). The microreactor was located in the isothermal zone of an electric furnace. A K-type thermocouple immersed in the catalytic bed was employed to control and monitor the temperature of the bed during the runs. Mass flow controllers were used to feed the desired amounts of reactants to the reactor. All of the lines before and after the reactor were heated to 130 °C in order to prevent condensation. The products of the reactions performed were analysed through gas chromatography–mass spectrometry (GC-MS). Percent conversions were determined from the integrated GC-MS peak areas with corrections for the MS ionization cross-section as previously described.[64] For the methanol oxidation, the reaction products are methyl formate and CO_2, with some water as a byproduct. For the toluene oxidation reaction, the reaction product is CO_2, with some water as a byproduct as well. The total flow of reactants (O_2, He, toluene/methanol) was kept constant at 50 mL min^{-1}.

Author contributions

A. V. S.: project administration, supervision, formal analysis, investigation, writing – original draft, writing – review & editing, data curation, visualisation; C. T. Y. Z.: conceptualization, data curation, formal analysis, investigation, methodology, project administration, resources, supervision, validation, visualisation, writing – review & editing; N. K. M.: formal analysis, writing – original draft, writing – review & editing, visualisation; V. C. T. M. P.: data curation, formal analysis, investigation, writing – original draft, visualisation, validation; E. S.: conceptualization, data curation, investigation, methodology, supervision, validation; N. J. N.: formal analysis, writing review & editing; G. K. P.: formal analysis, writing – review & editing, visualisation; J. A.: conceptualization, funding acquisition, project administration, resources, software, writing – review & editing.

Data Availability

All data is provided within the manuscript and acquired using established techniques.

Conflicts of interest

There are no conflicts of interest to declare.

Acknowledgements

This work was supported by the U.S. Defense Threat Reduction Agency (DTRA) under Award Number HDTR12110016. N.K.M. was funded by an Internationalisation Fellowship from the Carlsberg Foundation (CF21-0614). We would like to thank Dr Daniel Daniel for contributing to the project conceptualization, previous microscopy developments, and discussions; Dr Tanya Shirman for discussions and providing the methodology for raspberry colloid preparation and assembly; Dr Judy Lattimer and Dr Yamin Htet for helping with the catalysis experiments; Dr Danieli Foresti for guidance regarding the droplet deposition; Dr Nadir Kaplan, Dr Michael Kreder, and Garrick Lim for discussions; Paul Cassé for general experimental assistance; and Dr Haichao Wu for critical feedback on the manuscript.

Notes and references

1 S. Wintzheimer, T. Granath, M. Oppmann, T. Kister, T. Thai, T. Kraus, N. Vogel and K. Mandel, *ACS Nano*, 2018, **12**, 5093–5120.
2 Y. Ma, C. Cortez-Jugo, J. Li, Z. Lin, R. T. Richardson, Y. Han, J. Zhou, M. Björnmalm, O. M. Feeney, Q.-Z. Zhong, C. J. H. Porter, A. K. Wise and F. Caruso, *Biomacromolecules*, 2019, **20**, 3425–3434.
3 Y. Ma, M. Björnmalm, A. K. Wise, C. Cortez-Jugo, E. Revalor, Y. Ju, O. M. Feeney, R. T. Richardson, E. Hanssen, R. K. Shepherd, C. J. H. Porter and F. Caruso, *ACS Appl. Mater. Interfaces*, 2018, **10**, 31019–31031.
4 J. Guo, W. Yang and C. Wang, *Adv. Mater.*, 2013, **25**, 5196–5214.
5 J. Reichstein, S. Schötz, M. Macht, S. Maisel, N. Stockinger, C. C. Collados, K. Schubert, D. Blaumeiser, S. Wintzheimer, A. Görling, M. Thommes, D. Zahn, J. Libuda, T. Bauer and K. Mandel, *Adv. Funct. Mater.*, 2022, **32**, 2112379.
6 S. Wenderoth, S. Müssig, J. Prieschl, E. Genin, K. Heuzé, F. Fidler, D. Haddad, S. Wintzheimer and K. Mandel, *Nano Lett.*, 2022, **22**, 2762–2768.
7 S. Kang, W. Wang, A. Rahman, W. Nam, W. Zhou and P. J. Vikesland, *RSC Adv.*, 2022, **12**, 32803–32812.

Published on 13 September 2024. Downloaded on 5/23/2026 4:22:31 AM.

8 J. E. S. Van Der Hoeven, H. Gurunarayanan, M. Bransen, D. A. M. De Winter, P. E. De Jongh and A. Van Blaaderen, *Adv. Funct. Mater.*, 2022, **32**, 2200148.
9 S. Xu, Z. Weng, J. Tan, J. Guo and C. Wang, *Polym. Chem.*, 2015, **6**, 2892–2899.
10 W. Liu, M. Kappl and H.-J. Butt, *ACS Nano*, 2019, **13**, 13949–13956.
11 S. Wintzheimer, J. Reichstein, P. Groppe, A. Wolf, B. Fett, H. Zhou, R. Pujales-Paradela, F. Miller, S. Müssig, S. Wenderoth and K. Mandel, *Adv. Funct. Mater.*, 2021, **31**, 2011089.
12 M. Schneider, A. Tschöpe, D. Hanselmann, T. Ballweg, C. Gellermann, M. Franzreb and K. Mandel, *Part Syst. Charact.*, 2020, **37**, 1900487.
13 N. Vogel, S. Utech, G. T. England, T. Shirman, K. R. Phillips, N. Koay, I. B. Burgess, M. Kolle, D. A. Weitz and J. Aizenberg, *Proc. Natl. Acad. Sci. U. S. A.*, 2015, **112**, 10845–10850.
14 R. Ohnuki, M. Sakai, Y. Takeoka and S. Yoshioka, *Langmuir*, 2020, **36**, 5579–5587.
15 J. Wang, Y. Liu, G. Bleyer, E. S. A. Goerlitzer, S. Englisch, T. Przybilla, C. F. Mbah, M. Engel, E. Spiecker, I. Imaz, D. Maspoch and N. Vogel, *Angew. Chem., Int. Ed.*, 2022, **61**, e202117455.
16 P. U. Alves, B. J. E. Guilhabert, J. R. McPhillimy, D. Jevtics, M. J. Strain, M. Hejda, D. Cameron, P. R. Edwards, R. W. Martin, M. D. Dawson and N. Laurand, *ACS Appl. Opt. Mater.*, 2023, **1**, 1836–1846.
17 N. Denkov, O. Velev, P. Kralchevski, I. Ivanov, H. Yoshimura and K. Nagayama, *Langmuir*, 1992, **8**, 3183–3190.
18 Q. Yan, L. Gao, V. Sharma, Y.-M. Chiang and C. C. Wong, *Langmuir*, 2008, **24**, 11518–11522.
19 S. Wenderoth, A. Eigen, S. Wintzheimer, J. Prieschl, A. Hirsch, M. Halik and K. Mandel, *Small*, 2022, **18**, 2107513.
20 M. Yu, C. Le Floch-Fouéré, L. Pauchard, F. Boissel, N. Fu, X. D. Chen, A. Saint-Jalmes, R. Jeantet and L. Lanotte, *Colloids Surf., A*, 2021, **620**, 126560.
21 Y. Chen, T. T. Mutukuri, N. E. Wilson and Q. (Tony) Zhou, *Adv. Drug Delivery Rev.*, 2021, **172**, 211–233.
22 A. Lechanteur and B. Evrard, *Pharmaceutics*, 2020, **12**, 55.
23 T. A. Yakhno and V. G. Yakhno, *Tech. Phys.*, 2009, **54**, 1219–1227.
24 O. Peschel, S. N. Kunz, M. A. Rothschild and E. Mützel, *Forensic Sci., Med., Pathol.*, 2011, **7**, 257–270.
25 M. Mukhopadhyay, R. Ray, M. Ayushman, P. Sood, M. Bhattacharyya, D. Sarkar and S. DasGupta, *J. Colloid Interface Sci.*, 2020, **573**, 307–316.
26 M. J. Hertaeg, R. F. Tabor, A. F. Routh and G. Garnier, *Phil. Trans. R. Soc. A.*, 2021, **379**, 20200391.
27 W. Shim, C. S. Moon, H. Kim, H. S. Kim, H. Zhang, S. K. Kang, P. S. Lee and S. Wooh, *Crystals*, 2021, **11**, 79.
28 V. Rastogi, S. Melle, O. G. Calderón, A. A. García, M. Marquez and O. D. Velev, *Adv. Mater.*, 2008, **20**, 4263–4268.
29 V. Rastogi, A. A. García, M. Marquez and O. D. Velev, *Macromol. Rapid Commun.*, 2010, **31**, 190–195.
30 D. Daniel, J. V. I. Timonen, R. Li, S. J. Velling, M. J. Kreder, A. Tetreault and J. Aizenberg, *Phys. Rev. Lett.*, 2018, **120**, 244503.
31 L. Chen and J. R. G. Evans, *J. Colloid Interface Sci.*, 2010, **351**, 283–287.
32 J. Heo, J. Lee, W. Shim, H. Kim, S. Fujii, J. Lim, M. Kappl, H.-J. Butt and S. Wooh, *ACS Appl. Mater. Interfaces*, 2023, **15**, 38986–38995.
33 C. López, *Adv. Mater.*, 2003, **15**, 1679–1704.
34 A. Osman, L. Goehring, A. Patti, H. Stitt and N. Shokri, *Ind. Eng. Chem. Res.*, 2017, **56**, 10506–10513.
35 W. Liu, M. Kappl, W. Steffen and H.-J. Butt, *J. Colloid Interface Sci.*, 2022, **607**, 1661–1670.
36 N. Tsapis, E. R. Dufresne, S. S. Sinha, C. S. Riera, J. W. Hutchinson, L. Mahadevan and D. A. Weitz, *Phys. Rev. Lett.*, 2005, **94**, 018302.
37 É. Lintingre, G. Ducouret, F. Lequeux, L. Olanier, T. Périé and L. Talini, *Soft Matter*, 2015, **11**, 3660–3665.
38 Á. G. Marín, H. Gelderblom, D. Lohse and J. H. Snoeijer, *Phys. Rev. Lett.*, 2011, **107**, 085502.
39 R. Mondal, H. Lama and K. C. Sahu, *Phys. Fluids*, 2023, **35**, 061301.
40 D. K. Makepeace, A. Fortini, A. Markov, P. Locatelli, C. Lindsay, S. Moorhouse, R. Lind, R. P. Sear and J. L. Keddie, *Soft Matter*, 2017, **13**, 6969–6980.
41 T.-S. Wong, T.-H. Chen, X. Shen and C.-M. Ho, *Anal. Chem.*, 2011, **83**, 1871–1873.
42 V. H. Chhasatia and Y. Sun, *Soft Matter*, 2011, **7**, 10135.
43 A. Fortini, I. Martín-Fabiani, J. L. De La Haye, P.-Y. Dugas, M. Lansalot, F. D'Agosto, E. Bourgeat-Lami, J. L. Keddie and R. P. Sear, *Phys. Rev. Lett.*, 2016, **116**, 118301.
44 J. Zhou, Y. Jiang and M. Doi, *Phys. Rev. Lett.*, 2017, **118**, 108002.
45 J. Wang, J. Schwenger, A. Ströbel, P. Feldner, P. Herre, S. Romeis, W. Peukert, B. Merle and N. Vogel, *Sci. Adv.*, 2021, **7**, eabj0954.
46 I. Prasad, C. Santangelo and G. Grason, *Phys. Rev. E*, 2017, **96**, 052905.
47 J. B. Rosenholm, *Adv. Colloid Interface Sci.*, 2023, **315**, 102887.
48 Z. Li, Q. Fan and Y. Yin, *Chem. Rev.*, 2021, **122**, 4976–5067.
49 T. Shirman, J. Lattimer, M. Luneau, E. Shirman, C. Reece, M. Aizenberg, R. J. Madix, J. Aizenberg and C. M. Friend, *Chem. A Eur. J.*, 2018, **24**, 1833–1837.
50 M. Luneau, T. Shirman, A. Filie, J. Timoshenko, W. Chen, A. Trimpalis, M. Flytzani-Stephanopoulos, E. Kaxiras, A. I. Frenkel, J. Aizenberg, C. M. Friend and R. J. Madix, *Chem. Mater.*, 2019, **31**, 5759–5768.
51 J. E. S. Van Der Hoeven, S. Krämer, S. Dussi, T. Shirman, K. K. Park, C. H. Rycroft, D. C. Bell, C. M. Friend and J. Aizenberg, *Adv. Funct. Mater.*, 2021, **31**, 2106876.
52 F. Moreau, G. Bond and A. Taylor, *J. Catal.*, 2005, **231**, 105–114.
53 P. N. Amaniampong, K. Li, X. Jia, B. Wang, A. Borgna and Y. Yang, *ChemCatChem*, 2014, **6**, 2105–2114.
54 S. Fountoulaki, P. L. Gkizis, T. S. Symeonidis, E. Kaminioti, A. Karina, I. Tamiolakis, G. S. Armatas and I. N. Lykakis, *Adv. Synth. Catal.*, 2016, **358**, 1500–1508.
55 G. Son, Y. Li, A. V. Shneidman, J. H. Han, M. Aizenberg, P. Sautet and J. Aizenberg, *Chem. Mater.*, 2023, **35**, 9505–9516.

 This journal is © The Royal Society of Chemistry 2024

56 J. H. Han, A. V. Shneidman, D. Y. Kim, N. J. Nicolas, J. E. S. Van Der Hoeven, M. Aizenberg and J. Aizenberg, *Angew. Chem., Int. Ed.*, 2022, **61**, e202111048.
57 S. Wooh, N. Encinas, D. Vollmer and H. Butt, *Adv. Mater.*, 2017, **29**, 1604637.
58 K. Tadanaga, N. Katata and T. Minami, *J. Am. Ceram. Soc.*, 2005, **80**, 1040–1042.
59 P. Kim, M. J. Kreder, J. Alvarenga and J. Aizenberg, *Nano Lett.*, 2013, **13**, 1793–1799.
60 T. Meincke and R. N. Klupp Taylor, *Particuology*, 2023, **75**, 137–150.
61 W. Shi, Y. Sahoo, M. T. Swihart and P. N. Prasad, *Langmuir*, 2005, **21**, 1610–1617.
62 V. Prasad, A. Mikhailovsky and J. A. Zasadzinski, *Langmuir*, 2005, **21**, 7528–7532.
63 A. Shaikeea, S. Basu, S. Hatte and L. Bansal, *Langmuir*, 2016, **32**, 10334–10343.
64 E. Shirman, T. Shirman, A. V. Shneidman, A. Grinthal, K. R. Phillips, H. Whelan, E. Bulger, M. Abramovitch, J. Patil, R. Nevarez and J. Aizenberg, *Adv. Funct. Mater.*, 2018, **28**, 1704559.

Published on 13 September 2024. Downloaded on 5/23/2026 4:22:31 AM.